Journal of Advanced Concrete Technology Vol. 21, 271-283, April 2023 / Copyright © 2023 Japan Concrete Institute

Scientific paper

A Micromechanics-based Study on Cracking Characteristics of Engineered Geopolymer Composite

Motohiro Ohno[1*] and Victor C. Li[2]

Received 5 September 2022, accepted 27 March 2023

doi:10.3151/jact.21.271

Abstract

This study aims at experimentally and analytically characterizing cracking characteristics of Engineered Geopolymer Composites (EGCs) and at identifying optimal combinations of micromechanical parameters for enhancing the composite tensile performance. Fly ash-based EGCs with different volume fractions of polyvinyl alcohol fibers are investigated. The number of cracks and residual crack widths are measured for EGC specimens uniaxially loaded to 1% and 2% tensile strain. The observed crack patterns are analyzed by a micromechanics-based model that relates matrix, fiber, and interface properties to the macroscopic composite behavior. The experimental results demonstrate the lognormal distributions of crack widths and more tightly controlled cracking compared to Engineered Cementitious Composites. The simulated fiber bridging stress-crack opening relationship (σ-δ relationship) suggests that relatively high chemical bond and low frictional bond lead to the tight crack width. The simulation results also suggest that the first-cracking strength and the subsequent micro-cracking stress during the hardening stage should be below the analytical σ-δ curve peak. Higher chemical bond is beneficial for meeting these conditions, but if it is too high, fiber rupture dominates over pull-out, which lowers the complementary energy. Lower frictional bond or slip-hardening coefficient can suppress the fiber rupture tendency.

1. Introduction

The use of low-carbon materials is not sufficient to realize sustainable buildings and civil infrastructure. While the carbon footprints in the production stage are reduced, it does not guarantee that the life-cycle greenhouse gas (GHG) emissions are minimized. Indeed, the use and end-of-life stages can have significant impacts on the life-cycle environmental assessment of concrete (Wu *et al.* 2014). For instance, maintenance and rehabilitation of concrete pavements cause a considerable amount of energy consumptions and GHG emissions (Chehovits and Galehouse 2010; Loijos 2011). In preventing frequent repairs/replacements and extending the service life, material durability plays an important role. Hence, the combination of enhanced material greenness and durability is essential for reducing life-cycle impacts of concrete structures.

As a green and durable construction material, High-Performance Fiber-Reinforced Geopolymer Composite (HPFRGC), also known as Strain-hardening Geopolymer Composite (SHGC) or Engineered Geopolymer Composite (EGC), is receiving increasing attention (Elmesalami and Celik 2022). This special type of fiber-reinforced geopolymer composites exhibits strain-hardening characteristics with high ductility under tension and flexure, as in Engineered Cementitious Composite (ECC) (Li 2003). The high tensile ductility results from multiple-cracking characteristics and tightly-controlled crack widths (Nematollahi *et al.* 2015; Ohno and Li 2014). Besides the unique mechanical properties, good durability properties such as high resistance to sulfuric acid (Ohno and Li 2019) and to sulfate attack (Salami *et al.* 2017), and self-healing capabilities (Guo *et al.* 2020; Kan *et al.* 2019; Ohno *et al.* 2020) have been reported. Embodied energy and GHG emissions of EGCs have also been investigated in previous studies (Nematollahi *et al.* 2017b; Ohno and Li 2018; Zhong and Zhang 2021), which demonstrated lower environmental impacts than ordinary Portland cement (OPC) concrete. In the past decade, much effort has been directed towards developing various types of EGCs, using a variety of fibers, precursors, alkaline activators, recycled materials, and curing methods. (Al-Majidi *et al.* 2017; Trindade *et al.* 2019; Khan and Ayub 2022; Nematollahi *et al.* 2017b; Wang *et al.* 2020, 2021).

Despite the burgeoning interest in EGCs, understanding of the cracking characteristics remains limited. Previous studies reported the number of cracks and crack widths under loading or after unloading (i.e., residual cracks) at failure (Kan *et al.* 2020; Li *et al.* 2021; Nematollahi *et al.* 2015, 2017a, 2017b; Nguyễn *et al.* 2021; Wang *et al.* 2020; Zhang *et al.* 2020); however, the evolution of crack patterns with strain was not provided. Predicting the number of cracks and crack widths at an arbitrary strain is important to evaluate the durability of the material. While the authors investigated the development of crack widths for an EGC (Ohno and Li 2014), available data are still scarce. Also, the underlying cause of the crack characteristics was not fully discussed in previous studies. In general, different matrices, fibers, and

---

[1] Project Assistant Professor, Department of Civil Engineering, The University of Tokyo, Japan.
*Corresponding author,
E-mail: ohno@concrete.t.u-tokyo.ac.jp
[2] Professor, Department of Civil and Environmental Engineering, University of Michigan, Ann Arbor, MI 48109-2125, USA.

Table 1 Mix designs of EGCs in kg/m^3 (ratios shown in parentheses).

Mix ID	Fly ash-1	Fly ash-2	Sand	Na_2SiO_3	NaOH	Water	Mix water	PVA fiber
EGC V_f1.5	694 (0.600)	463 (0.400)	463 (0.400)	260 (0.225)	60 (0.052)	27 (0.023)	116 (0.100)	19.5 (0.023)
EGC V_f2.0	691 (0.600)	460 (0.400)	460 (0.400)	259 (0.225)	60 (0.052)	27 (0.023)	115 (0.100)	26 (0.017)

their combinations result in different cracking patterns. Therefore, effects of micromechanical parameters (i.e., matrix, fiber, and interface properties) on EGC cracking characteristics need to be studied.

Li and Leung (1992) first proposed a micromechanics-based approach that relates micromechanical parameters to the macroscopic behavior of short fiber-reinforced composites. Later, various modifications and extensions of the model have been made, and the model developed by Yang *et al.* (2008) is currently used by many researchers. In the micromechanics-based model, the constitutive law of the fiber bridging stress-crack opening relationship (so called σ-δ relationship) is expressed as:

$$\sigma(\delta)=\frac{V_f}{A_f}\int_0^{\frac{\pi}{2}}\int_0^{(L_f/2)\cos\varphi}P(\delta,L_e)\,g(\varphi)\,p_1(\varphi)\,p_2(z)\,dz\,d\varphi \qquad (1)$$

where V_f is the fiber volume fraction; A_f is the cross-sectional area of fiber; φ is the fiber inclination angle with respect to the normal of the crack plane; L_f is the fiber length; z is the distance between the fiber centroid and the crack plane; L_e is the fiber embedment length; $P(\delta, L_e)$ represents the load carried by a single fiber aligned normal to the crack plane (i.e., φ=0); $g(\varphi)$ is a function to take into account the additional frictional force occurring at the exit point of the inclined fiber from the matrix (i.e., snubbing effect); $p_1(\varphi)$ and $p_2(z)$ are probability density functions of φ and z, which account for the random distribution of fibers in the composite. The complete derivations and mathematical expressions for $P(\delta, L_e)$, $g(\varphi)$, $p_1(\varphi)$ and $p_2(z)$ can be found elsewhere (Ohno 2017). In essence, micromechanical parameters govern the single fiber bridging force and the resultant composite σ-δ relationship. Then, the simulated σ-δ curve is used to judge whether the following two necessary conditions for steady-state multiple cracking are satisfied (Yang *et al.* 2008):

$$\sigma_c \le \sigma_0 \qquad (2)$$

$$J_{tip} \le \sigma_0\delta_0 - \int_0^{\delta_0}\sigma(\delta)\,d\delta \equiv J_b' \qquad (3)$$

where σ_c is the matrix tensile strength; σ_0 and δ_0 are the maximum fiber bridging strength and the corresponding crack opening; J_{tip} is the crack tip toughness; matrix tensile strength; J_b' is the complementary energy of the bridging fibers.

As indicated in Eq. (1), the micromechanical model can predict the crack opening δ (i.e., crack width) at an arbitrary composite stress σ based on given matrix, fiber, and interface properties. Thus, crack patterns of EGCs can be related to their micromechanical parameters from the simulation. Moreover, the effect of each parameter on the crack width can be evaluated by conducing sensitivity analyses. This enables identifying the combinations of matrix, fiber, and interface properties to ensure the tightly-controlled cracking and high durability of EGCs.

The objective of this study is to characterize cracking characteristics of EGCs experimentally and analytically, and to identify optimal micromechanical parameters for enhancing the composite tensile performance. Rectangular coupon specimens are prepared and subjected to uniaxial tension. The number of cracks and residual crack widths are measured for 1% and 2% tensile strain, and the evolution of the crack patterns with strain is analyzed based on probability distributions of the crack widths. Then, the σ-δ curves of the EGCs are simulated using the micromechanical model and their micromechanical parameters. The crack pattern evolution and the σ-δ relationship are compared with those of ECCs, and significant factors causing the differences are identified. In addition, sensitivity analyses are conducted for the EGC, varying micromechanical parameters. The simulation results suggest appropriate combinations of parameters for enhancing the EGC performance.

2. Materials and methods

2.1 Materials and mix proportions

Fly ash-based EGCs with different fiber contents were used in this study. **Table 1** lists the ingredients and the mix proportions, which were designed in a previous study (Ohno and Li 2018) based on an integrated design method for EGCs such that the good compressive strength, high tensile ductility, and low carbon footprints can be simultaneously achieved. The fiber volume fractions of EGC V_f1.5 and EGC V_f2.0 are 1.5% and 2.0%, respectively.

Two types of fly ash, labeled Fly ash-1 and Fly ash-2, were blended in the mixture to control the hardening property of geopolymer mortar. When the Fly ash-1 was singly used as the reactant, specimens did not harden enough and fractured in demolding one day after casting. On the other hand, the use of Fly ash-2 resulted in too fast setting time to cast in molds. These problems are likely to be related to the different amounts of CaO content, although both are classified as class F fly ash as designated by ASTM C618 (ASTM 2015). **Table 2** lists the chemical compositions of each fly ash reported from the manufacturer. The density and fineness (percent retained on 45 μm sieve) are 2.58 g/cm^3 and 22.24% for Fly ash-1, and

Table 2 Chemical compositions of two types of fly ash (mass %).

ID	SiO_2	Al_2O_3	Fe_2O_3	CaO	SO_3	MgO	Na_2O	K_2O	Moisture	LOI
Fly ash-1	46.09	23.15	19.48	5.08	0.77	1.12	0.58	1.73	0.16	1.99
Fly ash-2	42.20	22.51	9.20	15.66	1.85	3.20	0.98	1.53	0.12	1.34

Table 3 Properties of PVA fibers.

Nominal strength (MPa)	Apparent strength* (MPa)	Diameter (μm)	Length (mm)	Young's modulus (GPa)	Elongation (%)
1620	1092	39	12	42.8	6.0

*Strength of fibers embedded in a cement matrix, which is known to be lower than that in standard fiber strength testing (Kanda and Li 1998).

2.53 g/cm^3 and 16.58% for Fly ash-2. F-75 Ottawa silica sand was used as aggregate. The alkaline activator was prepared by dissolving laboratory-grade sodium hydroxide (NaOH) pellets in mixture of sodium silicate solution (Na_2SiO_3 with 8.9 wt% Na_2O, 28.7 wt% SiO_2, and 62.5 wt% H_2O) and tap water. The solution preparation was done at least 24 hours before its use as the activator so that chemical and thermal equilibrium was ensured. Additional water (labeled "Mix water" in **Table 1**) was used during mortar mixing to obtain desired rheology of the fresh mortar for achieving good fiber dispersion. Polyvinyl alcohol (PVA) fibers with 1.2% oil coating by weight were employed. The physical properties of the PVA fibers are listed in **Table 3**.

2.2 Specimen preparation

Fly ash and silica sand were dry mixed for 2 min. The activator solution and mix water were then added to the mixture, and mixing was continued until the mortar reached the desired fresh state. PVA fibers were slowly added to the mortar and mixed until the fibers were properly dispersed. The mixture was then cast into 305×76×12.7 mm (12×3×0.5 inch) prism molds (**Fig. 1**). The molds were designed so that specimens had smooth molded surfaces on the two 305×76 mm faces, which were convenient for attaching jigs for uniaxial tension tests. It should be noted, however, that casting and compaction into the mold are more difficult than into a regular mold for plate specimens. To achieve good compaction, molds were placed on a vibration table during casting, and additional manual compaction was applied to the fresh mixture by using a mallet.

Six coupon specimens were prepared for each series. All specimens were demolded 24 hours after casting and then oven-cured at 60°C for additional 24 hours. Subsequently, the specimens were cured at a room temperature (23±3°C) until the age of 28 days. After curing, the specimens were cut to 180 mm in length so as to minimize edge effects and bending stress that could occur in uniaxial tension tests. Prior to the loading, aluminum plates were glued to both ends of the specimens so as to facilitate the gripping of the specimens by the load frame.

2.3 Loading and crack width measurement

Three specimens in each series were uniaxially loaded to a tensile strain of 1% (named $V_f1.5–ε1$ and $V_f2.0–ε1$), and the other three specimens to 2% tensile strain (named $V_f1.5–ε2$ and $V_f2.0–ε2$). The test setup is shown in **Fig. 2(a)**. The loading was applied under displacement control at the rate of 0.5 mm/min, according to the recommendations of Japan Society of Civil Engineers for uniaxial tension tests on high-performance fiber-reinforced cement composites (JSCE 2008). Two LVDTs were attached to each specimen for measuring extensions within gauge length of about 80 mm. The tensile strain was computed

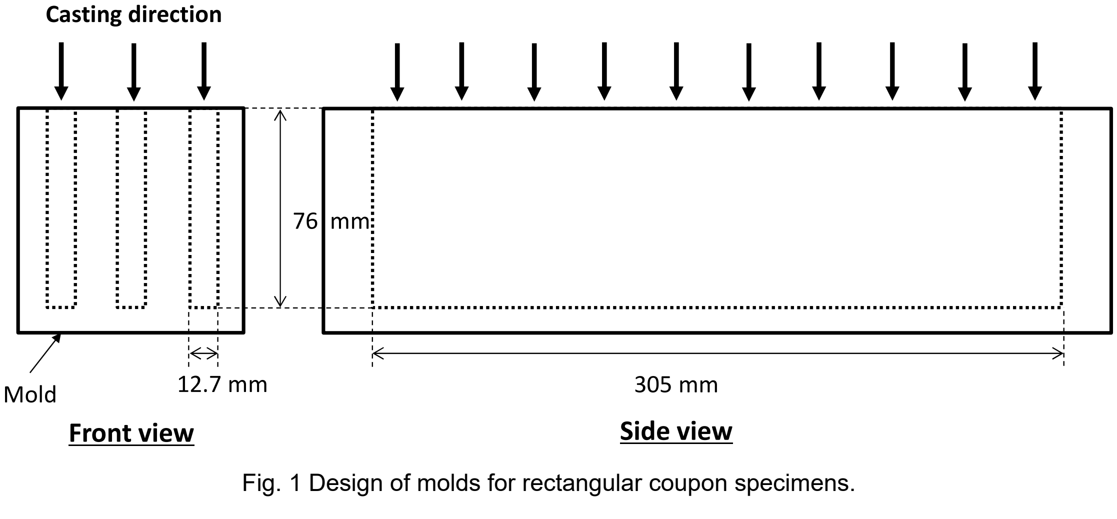

Fig. 1 Design of molds for rectangular coupon specimens.

Table 4 Simulation inputs (fiber properties are listed in Table 3).

ID	Chemical bond G_d (J/m^2)	Frictional bond τ_0 (MPa)	Slip-hardening coefficient β	Snubbing coefficient*	Strength reduction coefficient*	Fiber volume fraction (%)
EGC V$_f$1.5	6.10	0.70	0.33	0.2	0.33	1.5
EGC V$_f$2.0						2.0
ECC M45	1.26	2.66	0.40			2.0
HVFA ECC	0.55	3.37	0.42			2.0

*Assumed values based on another previous study (Yang *et al.* 2008).

from the average of extensions divided by the gauge length.

Once the desired strain level was reached in each specimen, the load was gradually removed to obtain the unloading stress-strain curve. The unloaded specimens were then observed by a digital optical microscope to record the number of microcracks and their residual crack widths. To accurately characterize the crack patterns, crack-width measurement was performed across three lines parallel to the loaded direction, which were drawn on the center and near the left and right edges of the specimen surface, as illustrated in **Fig. 2(b)**.

2.4 Analytical investigation

The model developed by Yang *et al.* (2008) was used to simulate the σ-δ relationship. The average fiber bridging stress-crack opening curve can be simulated for a crack plane with given matrix, fiber, and interface properties. Two-way fiber debonding/pullout is considered in the model, and there are 4 types of possible fiber status depending on the pullout load and displacement of each individual fiber:

(a) Two-way debonding (i.e., debonding at both embedment sides)
(b) Debonding at the long embedment side and fiber pullout at the short embedment side
(c) Two-way fiber pullout
(d) Fiber rupture

Once a crack is initiated at a plane, debonding occurs at both sides of the bridging fibers. When the crack opening reaches a threshold value for each fiber, debonding is completed at the short embedment side, in which the fiber starts to be pulled out with only interfacial friction. Subsequently, two-way fiber pullout occurs after complete debonding at the long embedment side. Fiber rupture occurs if the fiber pullout stress is greater than the apparent fiber strength.

Regarding other simulation configurations, two dimensional fiber distributions were assumed because of the small thickness of the coupon specimens. Matrix micro-spalling and Cook-Gordon effects were not considered in this study. These effects do not have remarkable impacts on the simulated σ-δ curve when PVA fibers are employed (Yang *et al.* 2008).

Simulations were conducted for EGC V$_f$1.5, EGC V$_f$2.0, and for two types of ECC: a standard ECC called M45 (Wang and Li 2007) and high volume fly ash ECC (HVFA ECC) (Yang *et al.* 2007). All series used the same type of PVA fibers. Micromechanical parameters of the EGCs studied here were measured and reported in a previous study (Ohno and Li 2018). Those of the ECCs can be found in Ranade *et al.* (2014). **Table 4** lists the simulation inputs used for the simulations. **Figure 3** illustrates the flow of the analytical simulations.

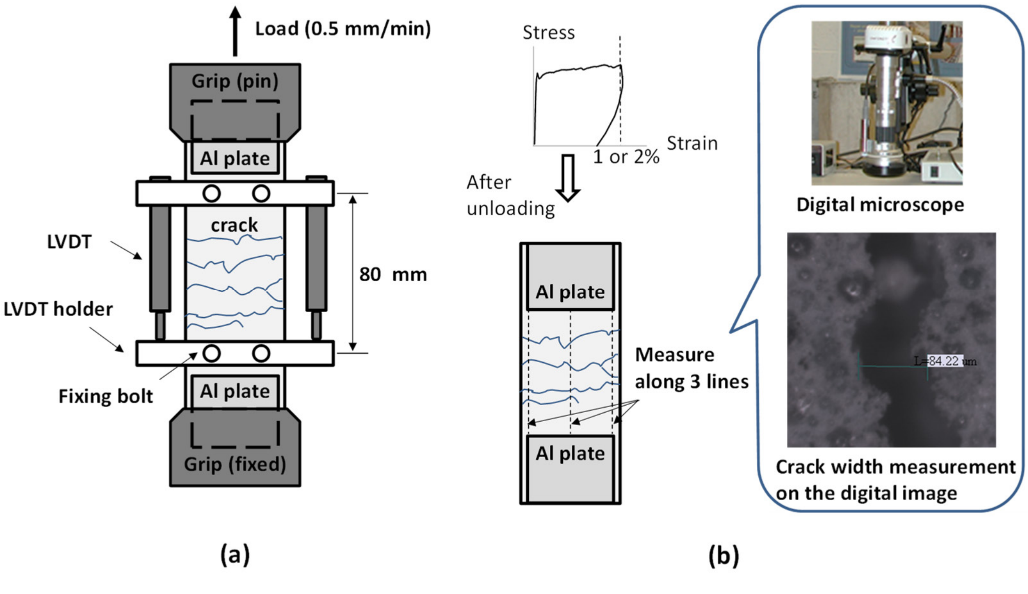

Fig. 2 Test setup for (a) uniaxial tension test and (b) crack measurement.

Table 5 Number of cracks and residual crack widths of EGCs.

Series	Specimen ID	Number of cracks			Maximum crack width (μm)	Average crack width (μm)
		Left edge	Center	Right edge		
V_f1.5–ε1	1	13	12	9	73.4	30.3
	2	8	14	10	66.8	24.6
	3	15	8	12	57.3	25.4
V_f1.5–ε2	1	16	15	12	779.9*	61.8
	2	15	16	19	156.0	38.6
	3	23	23	17	110.1	37.9
V_f2.0–ε1	1	13	12	22	78.8	16.5
	2	17	14	11	54.8	19.1
	3	17	19	15	351.0*	28.4
V_f2.0–ε2	1	25	36	17	770.4*	33.8
	2	24	22	28	61.4	22.8
	3	24	27	42	102.8	25.8

*A large, localized crack was observed, probably due to insufficient compaction.

3. Results and discussion

3.1 Experimental results

Figure 4 shows the tensile stress-strain curves of the EGC specimens. The strain-hardening behavior can be seen in all series. However, a localized crack was observed in some specimens during the loading. The unintended large cracking might be attributed to poor compaction and resultant large flaws in those specimens. Despite the localized damage, no significant variability is observed in their stress-strain curves in each series.

The stress-strain curves suggest that the fiber volume fraction affects the cracking characteristics; V_f1.5 series show larger load drops than V_f2.0 series during the strain-hardening stage. Slightly larger residual strains of V_f1.5 can also be seen in the 2% strain case. Both of these features imply that crack widths of V_f1.5 are larger than those of V_f2.0. Although the crack development was not visually recorded during the tensile tests, its tendency at different loading stages in each series is reflected in their load drops.

Table 5 presents the number of cracks and the crack widths. Overall, tightly-controlled multiple cracks are confirmed in most of the specimens, but as mentioned above, there are significantly large cracks in a few specimens. With those outliers included, the average crack width of V_f1.5 series is 1.3 times that of V_f2.0 series for 1% strain, and 1.7 times for 2% strain. This trend agrees with the observed larger load drops and residual strains in V_f1.5.

It should be noted that the number of cracks significantly varies among the center and near-edge areas of the specimen surface. This variation results from cracks that bifurcated during propagation and from cracks that did not fully propagate through the matrix. In addition, crack widths at the near-edge areas are mostly larger than those at the central area. Typically, crack width measurement for ECCs is performed on only the central longitudinal

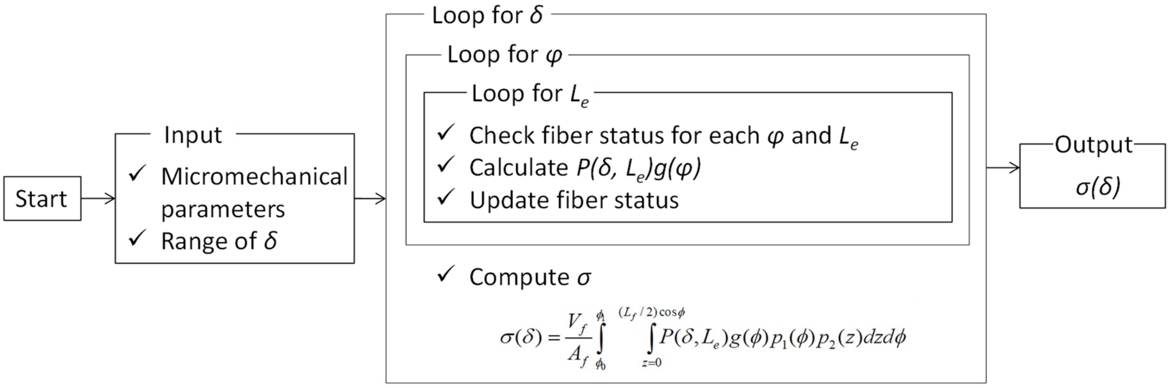

σ: Fiber-bridging stress
δ: crack opening
φ: Fiber inclination angle
L_e: Fiber embedment length
A_f: Fiber cross-sectional area
V_f: Fiber volume fraction

$P(\delta, L_e)$: Fiber-bridging force for given δ and L_e
$g(\varphi)$: Function to consider snubbing effect
$p_1(\varphi)$: Probability density function of φ
$p_2(z)$: Probability density function of fiber-centroid location

* Relevant equations can be found elsewhere (Yang et al. 2008)

Fig. 3 Flow of analytical simulation of σ-δ curve.

area (JSCE 2008), assuming that the crack opening is constant along each crack. However, the results here indicate that the assumption of a constant crack width is inappropriate for EGCs. Thus, multiple-point measurement for each crack is important to fully characterize the cracking characteristics.

To better illustrate EGC cracking characteristics, density histograms of crack widths and their fitted probability distributions are plotted in **Fig. 5**. The sample size N represents the total number of measurements on the center and near-edge areas of each specimen, excluding the outliers. The bin width of 10 μm is used as in previous studies on ECCs (Liu *et al.* 2016; Ranade *et al.* 2014). Lognormal distributions are well fitted to all series. When compared with $V_f2.0$ series, $V_f1.5$ series have larger standard deviations for both 1% and 2% strain levels, as well as the larger estimated means.

Lognormal distributions of crack widths have also been reported for ECCs in previous studies (Liu *et al.* 2016; Ranade *et al.* 2014; Wang *et al.* 2011) and are therefore regarded as general cracking characteristics of multiple-cracking fiber-reinforced brittle matrix composites. In addition, Ranade *et al.* (2014) demonstrated for ECC M45 and HVFA ECC that the mean (m) and the standard deviation (s) can be expressed as cubic functions of the applied tensile strain (ε):

$$m = C_3\varepsilon^3 + C_2\varepsilon^2 + C_1\varepsilon^1 + C_0 \tag{4}$$

$$s = K_3\varepsilon^3 + K_2\varepsilon^2 + K_1\varepsilon^1 + K_0 \tag{5}$$

where C_i and K_i (i= 0,1,2,3) are constant coefficients determined by regression analyses on experimental data. Then, two parameters (μ and σ') and the corresponding lognormal probability distribution function $p(\delta, \varepsilon)$ for a given crack width δ are calculated as follows:

$$\mu = ln\left(\frac{m^2}{\sqrt{s^2+m^2}}\right) \tag{6}$$

$$\sigma' = \sqrt{ln\left(\frac{s^2}{m^2}+1\right)} \tag{7}$$

$$p(\delta,\varepsilon) = \frac{1}{\delta\sigma'\sqrt{2\pi}}e^{\frac{-(ln\delta-\mu)^2}{2\sigma'^2}} \tag{8}$$

With these equations and the estimated parameters, the crack-width distribution at a given strain ε can be predicted.

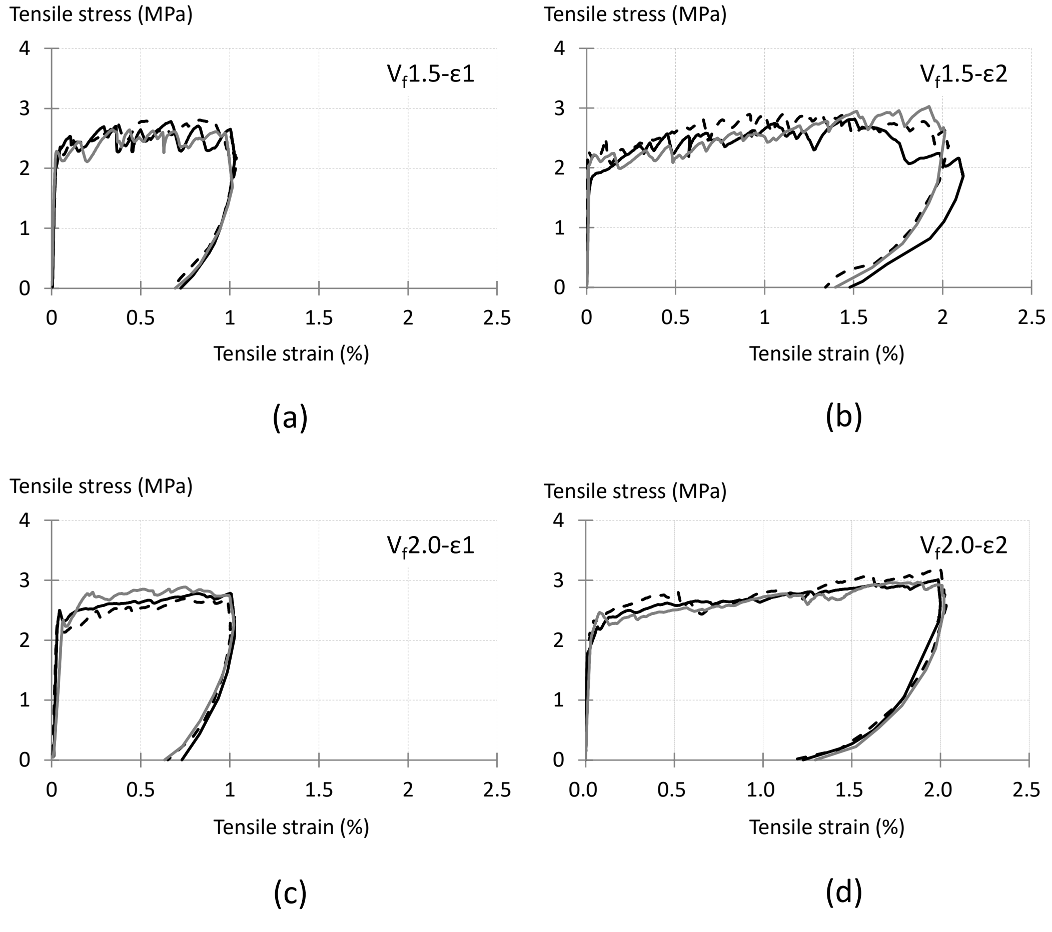

Fig. 4 Tensile stress-strain curves of (a), (b) EGC $V_f1.5$ and (c), (d) EGC $V_f2.0$ loaded to 1% or 2% strain. Three specimens were tested for each series.

It is worth comparing the crack-width distributions among EGCs and ECCs. The distributions at 1% and 2% strains for the ECCs can be estimated by using the Eqs. (4) to (8) and the reported coefficients. However, the data in Ranade *et al.* (2014) are crack widths under loading, while the residual crack widths after unloading were measured in this study. For a fair comparison, residual crack widths of the ECCs should be estimated. Here, the relationship observed by Li *et al.* (2001), that residual crack widths of PVA-ECCs were approximately 70% of the crack opening under loading, is used to convert the ECC data. It should be mentioned that 2% strain seems to be outside the applicable range of the Eqs. (1) and (2) for ECC M45 because the reported tensile strain capacity is smaller than 2% in most of the specimens in the series (Ranade *et al.* 2014). Hence, the comparison is done for only 1% strain.

Figure 6 shows the estimated probability distributions of residual crack widths at 1% strain. EGC V$_f$2.0 has the most right-skewed distribution with most cracks tightly controlled. The crack width at the mode (i.e., peak of the curve) of EGC V$_f$1.5 is slightly smaller than that of HVFA ECC, but the probability density is higher for crack widths larger than 37 μm. ECC M45 has the largest mean, and the distribution seems to be rather a normal distribution.

3.2 Analytical results

3.2.1 σ-δ relationship

The observed different cracking characteristics result

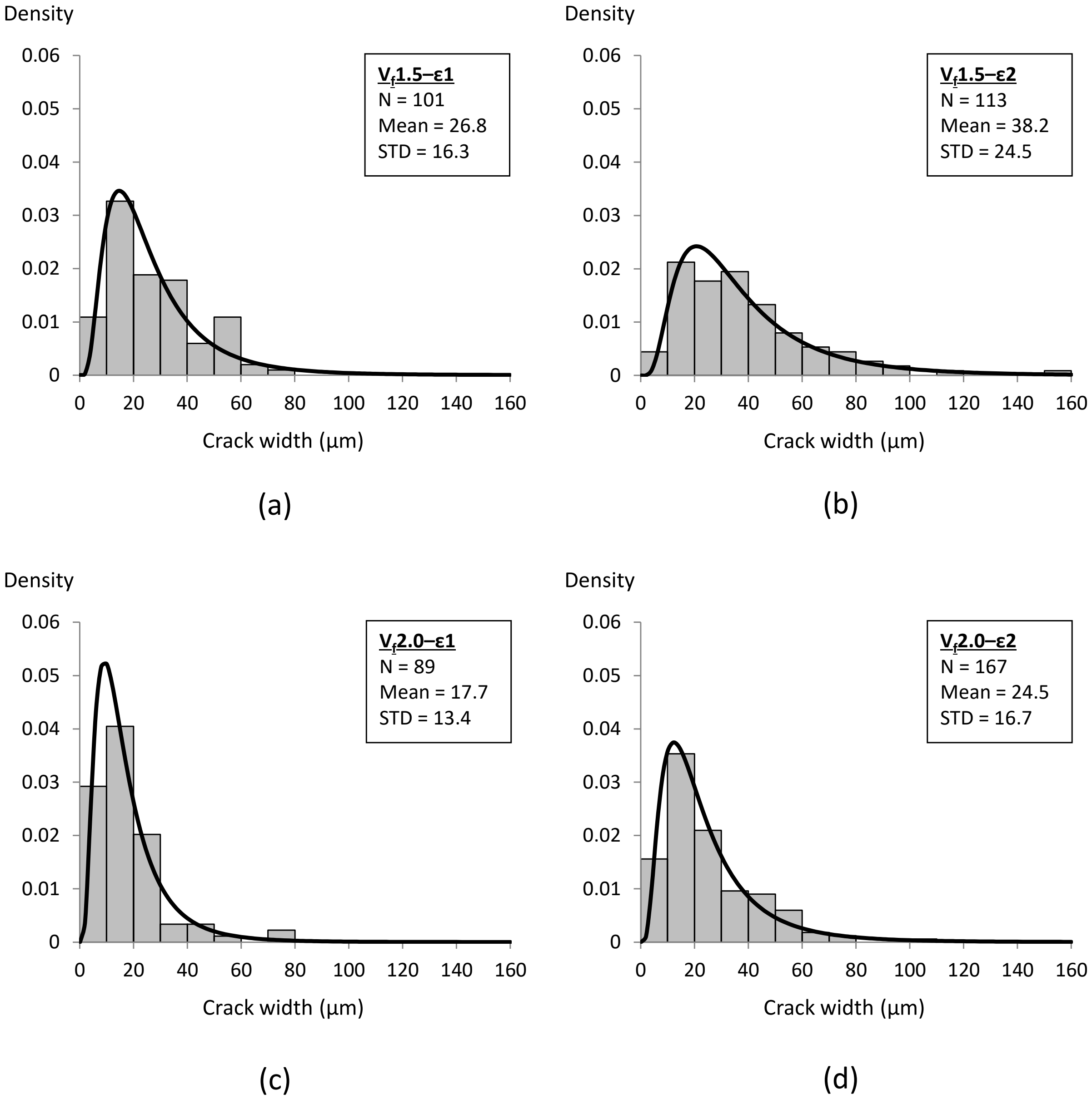

(a) (b) (c) (d)

Fig. 5 Density histograms of EGC crack widths and their fitted lognormal distributions.

from different properties of the matrix, fiber, and their interface. Here, each series is analyzed by the micromechanical model to investigate the cause of the differences.

Figure 7 shows the simulated σ-δ curves. Distinctly different behaviors can be seen among the series. In the ECCs, the fiber bridging stress reaches the peak at crack opening of about 30 μm and then monotonically decreases. On the other hand, the EGCs exhibit the first peak at about 60 μm and the maximum stress at about 200 μm. The underlying mechanics will be later discussed in this section. As a result of the unique σ-δ curves, the EGCs have remarkably larger complementary energy than the ECCs, which is beneficial for achieving steady-state flat crack propagation and robust strain-hardening characteristics. It should also be noted that the bridging stress at the zero crack opening (named σ_0) of the ECCs is 2-3 times smaller than those of the EGCs. For the ECCs, the bridging stress sharply increases toward the peak, while the EGCs show gentle stress increase and decrease for crack opening below 100 μm.

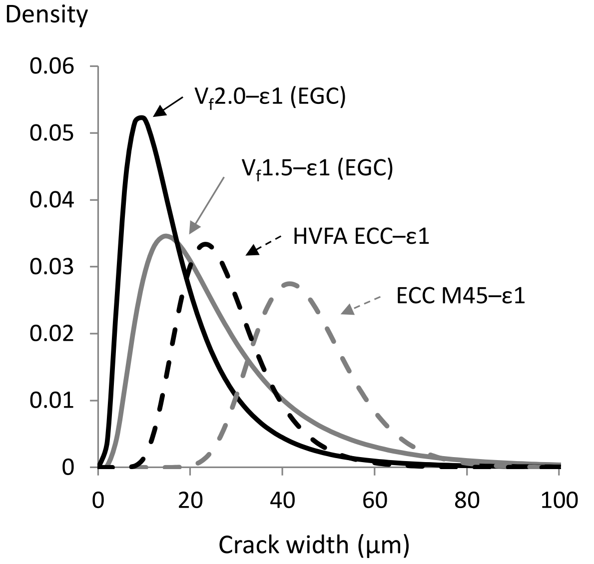

Fig. 6 Comparison of probability distributions of crack widths at 1% strain for EGCs and ECCs.

To investigate the source of the different cracking characteristics, the first-cracking strength (σ_{fc}) and the maximum stress observed by 1% tensile strain ($\sigma_{max\text{-}\varepsilon1}$) are plotted with the simulated σ-δ curve for each series (**Fig. 8**). Average values of 3 or 4 specimens are used for σ_{fc} and $\sigma_{max\text{-}\varepsilon1}$ In EGC V$_f$2.0, σ_{fc} and $\sigma_{max\text{-}\varepsilon1}$ lie under the simulated σ-δ curve. Theoretically, this means that, after the first crack is initiated in the plane, the crack opening is kept at zero as the bridging stress is smaller than the required stress for fiber debonding and pullout. It should be noted that the simulation uses average values of the measured micromechanical properties and assumes that the fibers are perfectly uniformly distributed, which would not be the case in actual specimens. Nevertheless, this result suggests that the crack opening can be considerably small in EGC V$_f$2.0. In the case of EGC V$_f$1.5, $\sigma_{max\text{-}\varepsilon1}$ is slightly higher than σ_0 but lies under the simulated σ-δ curve for almost the entire range. On the other hand, both σ_{fc} and $\sigma_{max\text{-}\varepsilon1}$ are larger than σ_0 in HVFA ECC and ECC M45, which implies that relatively large crack opening can occur. Therefore, it is suggested that tightly-controlled cracking can be achieved when the matrix tensile strength (corresponding to σ_{fc}) is lower than σ_0 and the macroscopic composite stress during the strain-hardening stage lies under the simulated σ-δ curve.

The evolution of the fiber status also plays an important role in cracking characteristics. **Figure 9** shows the ratio of broken fibers versus crack opening for each series. In the ECCs, rupture of some fibers occurs at about 20 μm, and the broken fiber ratio then linearly increases. This implies that a considerable number of fibers were broken in the ECC specimens subjected to 1% tensile strain. In the EGCs, fiber rupture is limited for crack opening below 100 μm. As the broken fibers cannot contribute to the elastic recovery during unloading, residual crack widths in the ECCs are likely to be larger than those in the EGCs.

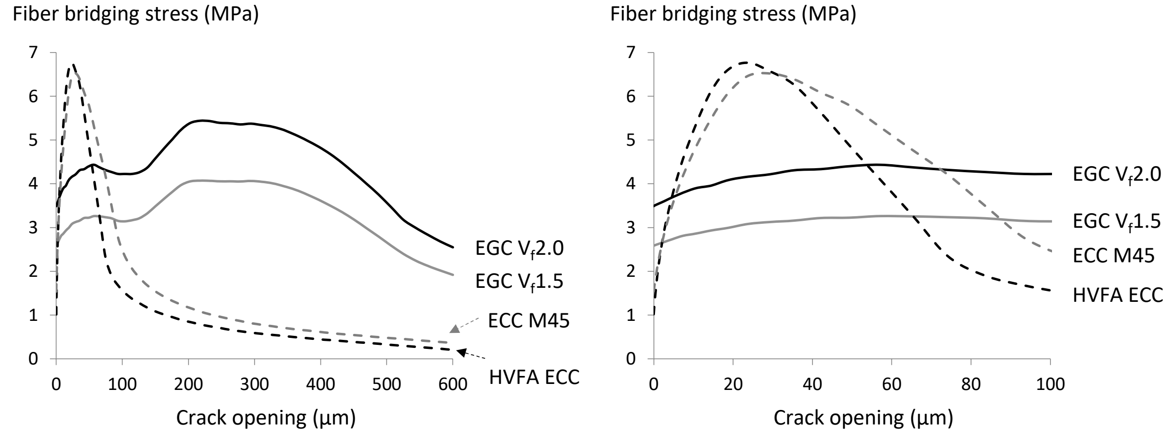

(a) (b)

Fig. 7 Simulated σ-δ curves: plots for crack opening below (a) 600 μm and (b) 100 μm.

The fiber status of the EGCs also explains their unique *σ*-*δ* relationships. The ratios of 2-way debonding fibers and broken fibers for EGC V$_f$2.0 are plotted with the *σ*-*δ* curve in **Fig. 10**. The three lines (A)(B)(C) in the graph correspond to the inflection points of the *σ*-*δ* curve. The fiber bridging stress keeps increasing up to (A) (crack opening of about 50 μm) and then slightly decreases as the fiber rupture occurs. Subsequently, the 2-way debonding ratio becomes zero at (B), and the stress starts to rise again. During this stage, the broken fiber ratio is almost constant. The reason of the stress increase is that the fiber pullout load of the debond-pullout stage tends to

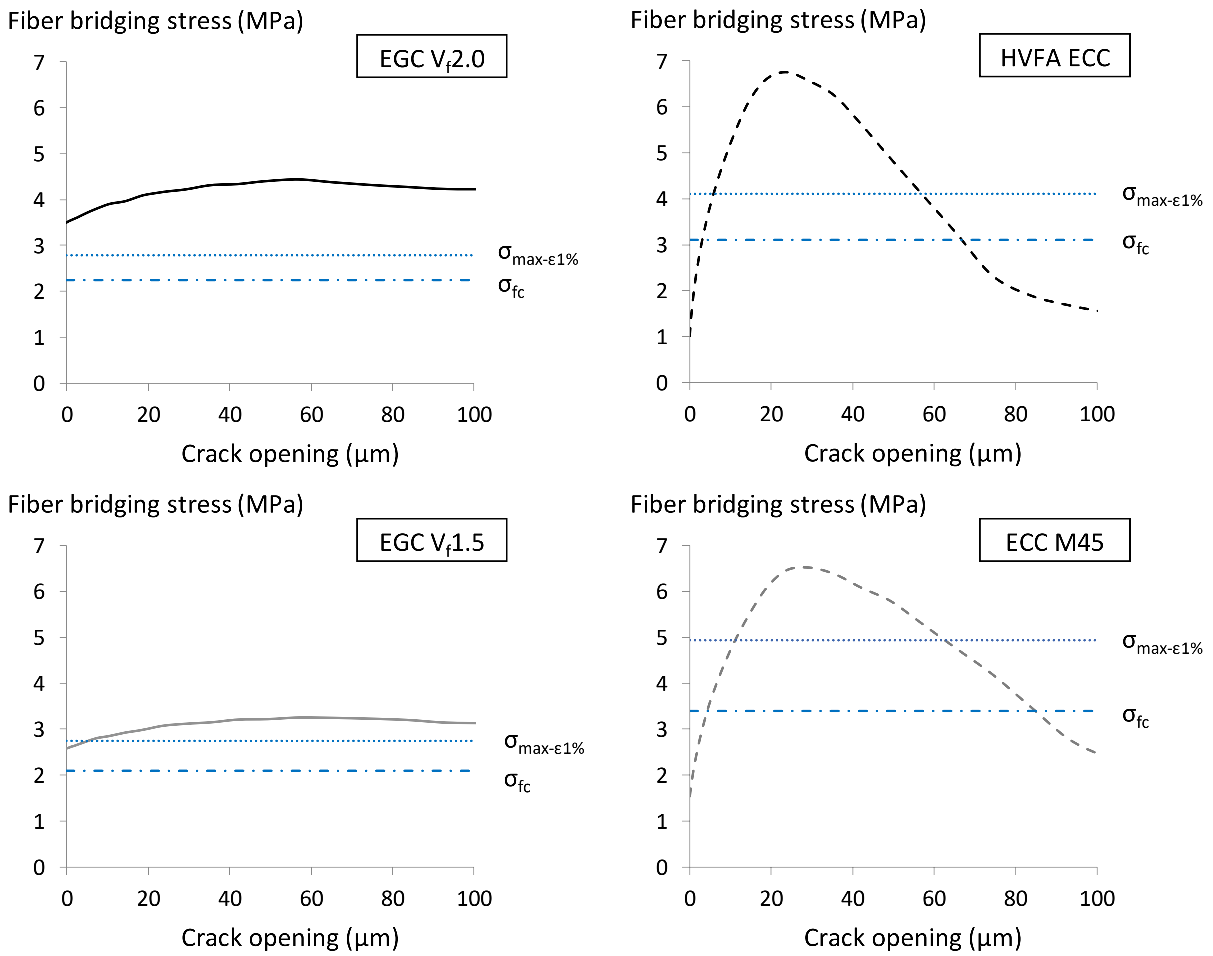

Fig. 8 First cracking strength and maximum stress observed by 1% strain plotted with simulated *σ*-*δ* curve for each series.

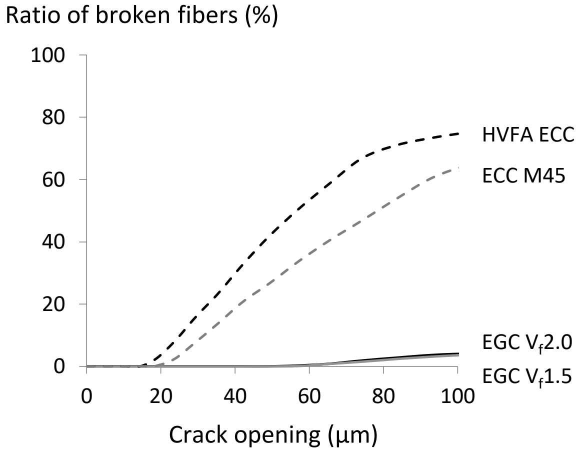

Fig. 9 Ratio of broken fibers versus crack opening for each series.

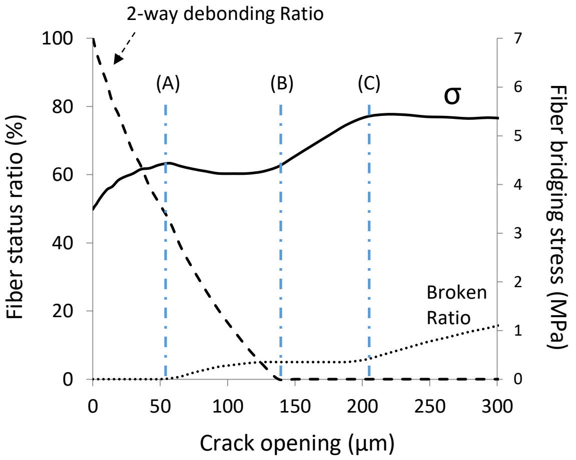

Fig. 10 Ratios of 2-way debonding fibers and broken fibers plotted with the *σ*-*δ* curve for EGC V$_f$2.0.

be higher than that of the 2-way debonding stage in the PVA-ECCs; PVA fibers typically exhibit slip-hardening behaviors due to an fiber abrasion and jamming effect during sliding of the fiber in the matrix tunnel (Yang *et al.* 2008). During the stage between (B) and (C), most fibers are in the debond-pullout stage and the fiber bridging stress keeps increasing due to the slip-hardening effect. When the crack opening is larger than 200 μm, the pullout stress reaches the apparent strength in some fibers, and the broken fiber ratio starts to increase again. As a result, the fiber bridging stress shows the maximum at (C) and then gradually decreases.

3.2.1 Sensitivity analyses

The discussions above suggest that cracking characteristics and the σ-δ relationship result from the complex combinations of matrix, fiber, and interface properties and of the resultant fiber status. To understand the effect of each micromechanical parameter, sensitivity analyses are conducted, varying the chemical bonding (G_d), frictional bond (τ_0), and slip-hardening coefficient (β). The range of each parameter is from half to twice the original value.

Figure 11 shows the simulation results. Regarding G_d, a stronger chemical bond leads to a higher σ_0, which is

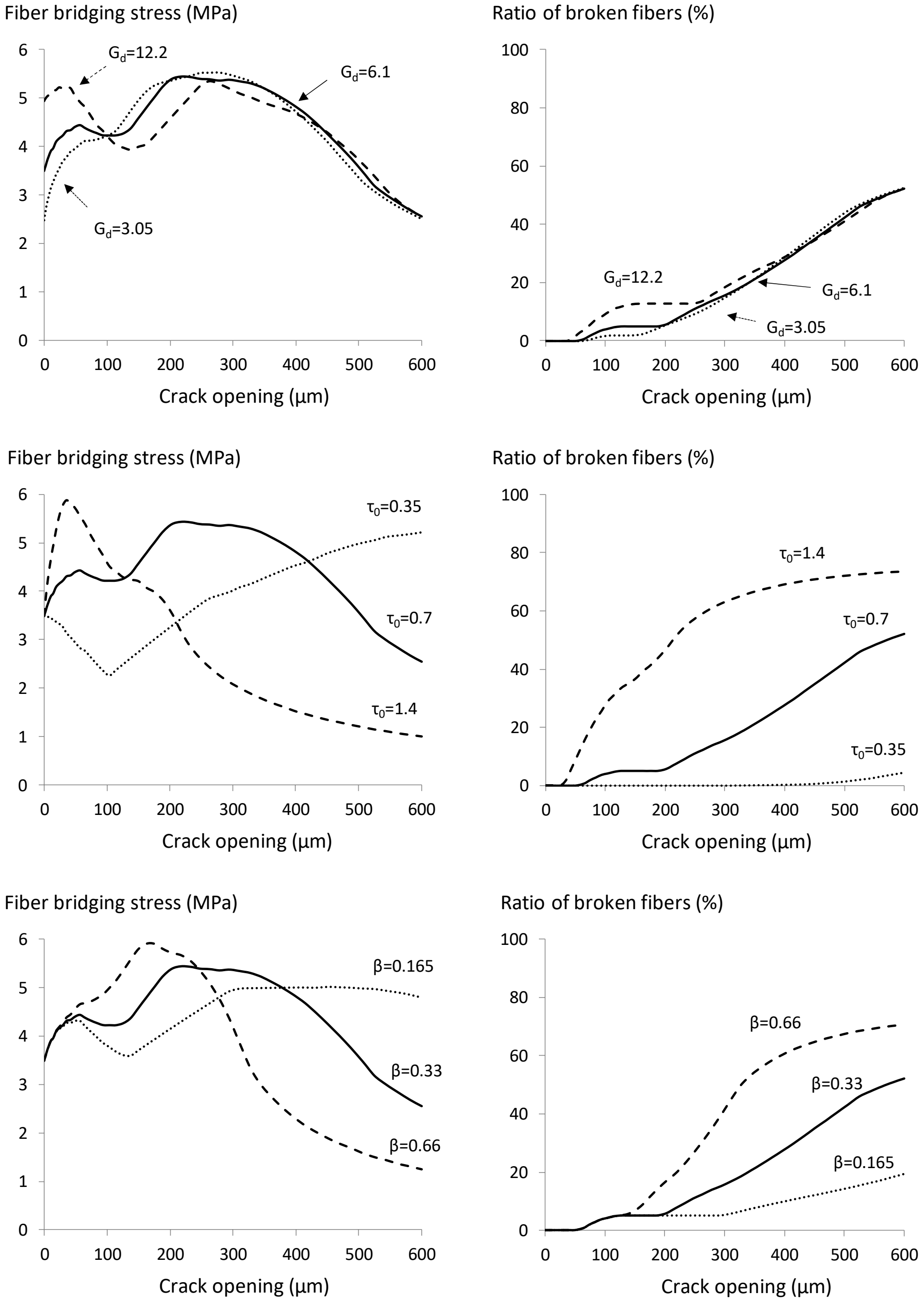

Fig. 11 σ-δ curves and ratios of broken fibers for EGC V_f2.0 with various values of chemical bond (G_d), frictional bond (τ_0), and slip-hardening coefficient β.

beneficial for tightly controlling crack widths as discussed above; however, if G_d is too high, more fibers are likely to be broken, and the fiber bridging stress would be lowered for larger crack widths. This could result in a smaller complementary energy. For τ_0, the σ-δ relationship seems to significantly differ depending on the frictional bond; twice τ_0 leads to a higher peak stress, but the fiber bridging stress then monotonically decreases without showing a secondary peak, and as a result, the complementary energy is limited. This can be related to the remarkably higher ratio of broken fibers. On the other hand, the bridging stress with a half of τ_0 exhibits no distinct peak but rather shows the minimum at crack opening of about 100 μm. It is difficult to appropriately define the complementary energy for this behavior, and further investigations would be needed to understand the influence on strain-hardening characteristics. In the case of the slip-hardening coefficient, doubling β results in a higher peak stress but the bridging stress is limited for larger crack widths, which is related to the higher ratio of broken fibers. On the other hand, reducing β by half shows higher bridging stress for larger crack widths as the fiber rupture is limited. These trends for β are similar to those for τ_0.

According to the simulation results, appropriate modifications on micromechanical parameters can be suggested for ensuring the high performance of EGCs. First, chemical bond should be sufficiently high to ensure that σ_{fc} is lower than σ_0. This is especially important when the high strength geopolymer matrix is employed. It should be noted that the complementary energy can be lowered if the chemical bond is too high. In that case, frictional bond or slip-hardening coefficient should be lowered to prevent fiber rupture and ensure the high complementary energy.

4. Conclusions

This study investigated, both experimentally and analytically, cracking characteristics of EGCs. The following conclusions can be drawn:

(1) The experimental characterization of EGC crack patterns indicates that the number of cracks and crack widths should be measured not only at the central longitudinal area but also at near-edge areas. Some cracks can bifurcate during propagation and/or cannot fully propagate through the matrix. This can cause significant variability in the crack-width measurement.

(2) The observed crack patterns also suggest that lognormal distributions of crack widths seem to be general cracking characteristics of multiple-cracking fiber-reinforced brittle matrix composites. Although EGCs and ECCs are different in the binder type and the fiber-matrix interface properties, crack widths are lognormally distributed in both cases.

(3) The micromechanics-based analytical simulations imply that, to achieve considerably tight cracking, the first-cracking strength and the subsequent macroscopic composite stress during the hardening stage should be lower than the peak of the analytical σ-δ relationship.

(4) The simulation results also indicate that higher chemical bond is beneficial for meeting the above conditions. However, if the chemical bond is too high, fiber rupture dominates, which lowers the complementary energy. Lower frictional bond or slip-hardening coefficient suppresses fiber rupture.

(5) Cracking characteristics of EGCs and ECCs seem to result from complex combinations of the matrix, fiber, and interface properties and of the resultant fiber status. The micromechanical model can evaluate the effect of each micromechanical parameter and predict the resultant σ-δ curve, which enables the identification of appropriate parameter modifications for performance assurance.

Further investigations are needed on effects of design variables (e.g., ingredients, mix proportions, curing conditions, etc.) on each micromechanical parameter. For example, identifying factors that lead to higher chemical bond, understanding the mechanism, and quantifying the effect are important. This will be the scope of the future study.

Acknowledgments

This work was supported by the National Science Foundation (Grant CMMI 1068005 to the University of Michigan) and the support is gratefully acknowledged.

References

Al-Majidi, M. H., Lampropoulos, A. and Cundy, A. B., (2017). "Tensile properties of a novel fibre reinforced geopolymer composite with enhanced strain hardening characteristics." *Composite Structures*, 168, 402-427.

ASTM, (2015). "*Standard specification for coal fly ash and raw or calcined natural pozzolona for use in concrete* (ASTM C618)." West Conshohocken, Pennsylvania, USA: ASTM International.

Chehovits, J. and Galehouse, L., (2010). "Energy usage and greenhouse gas emissions of pavement preservation processes for asphalt concrete pavements." In: *Compendium of Papers from the First International Conference on Pavement Preservation*, Newport Beach, California, USA 13-15 April 2010. Washington DC: US Federal Highway Administration, 27-42.

Elmesalami, N. and Celik, K., (2022). "A critical review of engineered geopolymer composite : A low-carbon ultra-high-performance concrete." *Construction and Building Materials*, 346, 128491.

Guo, X., Xiong, G. and Zhang, H., (2020). "In-situ evaluation of self-healing performance of engineered geopolymer composites (EGC) by ultrasonic method." *Materials Letters*, 280, 128546.

JSCE, (2008). "*Recommendations for design and construction of high performance fiber reinforced cement composites with multiple fine cracks*

(HPFRCC)." Tokyo: Japan Society of Civil Engineers.

Kan, L., Lv, J.-W., Duan, B.-B. and Wu, M., (2019). "Self-healing of engineered geopolymer composites prepared by fly ash and metakaolin." *Cement and Concrete Research*, 125, 105895.

Kan, L., Zhang, L., Zhao, Y. and Wu, M., (2020). "Properties of polyvinyl alcohol fiber reinforced fly ash based engineered geopolymer composites with zeolite replacement." *Construction and Building Materials*, 231, 117161.

Kanda, T. and Li, V. C., (1998). "Interface property and apparent strength of high-strength hydrophilic fiber in cement matrix." *Journal of Materials in Civil Engineering*, 10(1), 5-13.

Khan, S. U. and Ayub, T., (2022). "PET fiber-reinforced engineered geopolymer and cementitious composites." *Journal of Materials in Civil Engineering*, 34(3), 1-15.

Li, L., Sun, H. X., Zhang, Y. and Yu, B., (2021). "Surface cracking and fractal characteristics of bending fractured polypropylene fiber-reinforced geopolymer mortar." *Fractal and Fractional*, 5(4), 1-23.

Li, V. C., (2003). "On engineered cementitious composites (ECC). A review of the material and its applications." *Journal of Advanced Concrete Technology*, 1(3), 215-230.

Li, V. C. and Leung, C. K. Y., (1992). "Steady-state and multiple cracking of short random fiber composites." *Journal of Engineering Mechanics*, 118(11), 2246-2264.

Li, V. C., Wang, S. and Wu, C., (2001). "Tensile strain-hardening behavior of polyvinyl alcohol engineered cementitious composite (PVA-ECC)." *ACI Materials Journal*, 98(6), 483-492.

Liu, H., Zhang, Q., Gu, C., Su, H. and Li, V. C., (2016). "Influence of micro-cracking on the permeability of engineered cementitious composites." *Cement and Concrete Composites*, 72, 104-113.

Loijos, A., (2011). "*Life cycle assessment of concrete pavements: Impacts and opportunities*." Thesis (MSc). Massachusetts, USA: Massachusetts Institute of Technology.

Nematollahi, B., Qiu, J., Yang, E. H. and Sanjayan, J., (2017a). "Micromechanics constitutive modelling and optimization of strain hardening geopolymer composite." *Ceramics International*, 43(8), 5999-6007.

Nematollahi, B., Sanjayan, J. and Shaikh, F. U. A., (2015). "Tensile strain hardening behavior of PVA fiber-reinforced engineered geopolymer composite." *Journal of Materials in Civil Engineering*, 27, 04015001.

Nematollahi, B., Sanjayan, J., Qiu, J. and Yang, E. H., (2017b). "Micromechanics-based investigation of a sustainable ambient temperature cured one-part strain hardening geopolymer composite." *Construction and Building Materials*, 131, 552-563.

Nguyễn, H. H., Lương, Q. H., Choi, J.-I., Ranade, R., Li, V. C. and Lee, B. Y., (2021). "Ultra-ductile behavior of fly ash-based engineered geopolymer composites with a tensile strain capacity up to 13.7%." *Cement and Concrete Composites*, 122, 104133.

Ohno, M., (2017). "*Green and durable geopolymer composites for sustainable civil infrastructure*." Thesis (PhD). University of Michigan.

Ohno, M. and Li, V. C., (2014). "A feasibility study of strain hardening fiber reinforced fly ash-based geopolymer composites." *Construction and Building Materials*, 57, 163-168.

Ohno, M. and Li, V. C., (2018). "An integrated design method of engineered geopolymer composite." *Cement and Concrete Composites*, 88, 73-85.

Ohno, M. and Li, V. C., (2019). "Sulfuric acid resistance of strain hardening fibre reinforced geopolymer composite." *Indian Concrete Journal*, 93(12), 47-53.

Ohno, M., Kim, T. and Li, V. C., (2020). "Self-healing capability of strain-hardening fiber reinforced geopolymer composites." In: B. Zhao and X. Lu, Eds. *Proc. 17th fib Symposium on Concrete Structures for Resilient Societies*, Shanghai, China 22-24 November 2020. Lausanne, Switzerland: Fédération Internationale du Béton, 68-75.

Ranade, R., Zhang, J., Lynch, J. P. and Li, V. C., (2014). "Influence of micro-cracking on the composite resistivity of engineered cementitious composites." *Cement and Concrete Research*, 58, 1-12.

Salami, B., Johari, M., Ahmad, Z. and Maslehuddin, M., (2017). "Durability performance of palm oil fuel ash-based engineered alkaline-activated cementitious composite (POFA-EACC) mortar in sulfate environment." *Construction and Building Materials*, 131, 229-244.

Trindade, A. C. C., Borges, P. H. R. and Silva, F. A., (2019). "Mechanical behavior of strain-hardening geopolymer composites reinforced with natural and PVA fibers." *Materials Today: Proceedings*, 8(3), 753-759.

Wang, P., Wittmann, F. H., Zhao, T. and Huang, W., (2011). "Evolution of crack patterns on SHCC as function of imposed strain." In: R. D. Toledo Filho, F. A. Silva, E. A. B. Koenders and E. M. R. Fairbairn, Eds. *Proc. 2nd International RILEM Conference on Strain Hardening Cementitious Composites*, Rio de Janeiro, 12-14 December 2011. Paris, France: RILEM Publications, 217-224.

Wang, S. and Li, V. C., (2007). "Engineered cementitious composites with high-volume fly ash." *ACI Materials Journal*, 104(3), 233-241.

Wang, Y., Chan, C. L., Leong, S. H. and Zhang, M., (2020). "Engineering properties of strain hardening geopolymer composites with hybrid polyvinyl alcohol and recycled steel fibres." *Construction and Building Materials*, 261, 120585.

Wang, Y., Wang, Y. and Zhang, M., (2021). "Effect of sand content on engineering properties of fly ash-slag based strain hardening geopolymer composites." *Journal of Building Engineering*, 34, 101951.

Wu, P., Xia, B. and Zhao, X., (2014). "The importance of use and end-of-life phases to the life cycle greenhouse gas (GHG) emissions of concrete - A review." *Renewable and Sustainable Energy Reviews*, 37, 360-369.

Yang, E.-H., Wang, S., Yang, Y. and Li, V. C., (2008). "Fiber-bridging constitutive law of engineered cementitious composites." *Journal of Advanced Concrete Technology*, 6(1), 181-193.

Yang, E.-H., Yang, Y. and Li, V. C., (2007). "Use of high volumes of fly ash to improve ECC mechanical properties and material greenness." *ACI Materials Journal*, 104(6), 620-628.

Zhang, S., Li, V. C. and Ye, G., (2020). "Micromechanics-guided development of a slag/fly ash-based strain-hardening geopolymer composite." *Cement and Concrete Composites*, 109, 103510.

Zhong, H. and Zhang, M., (2021). "Effect of recycled tyre polymer fibre on engineering properties of sustainable strain hardening geopolymer composites." *Cement and Concrete Composites*, 122, 104167.